Available online at www.sciencedirect.com
ScienceDirect
Spectrochimica Acta Part A 69 (2008) 1372–1383
SPECTROCHIMICA ACTA PART A
www.elsevier.com/locate/saa

Radiation-induced defects in sucrose single crystals, revisited: A combined electron magnetic resonance and density functional theory study

H. De Cooman [a,b], E. Pauwels [b], H. Vrielinck [a], A. Dimitrova [c], N. Yordanov [c], E. Sagstuen [d], M. Waroquier [b], F. Callens [a,*]

[a] Department of Solid State Sciences, Ghent University, Krijgslaan 281-S1, B-9000 Gent, Belgium
[b] Center for Molecular Modeling, Ghent University, Proeftuinstraat 86, B-9000 Gent, Belgium
[c] Bulgarian Academy of Sciences, Lab EPR, Inst Catalysis, BU-1113 Sofia, Bulgaria
[d] Department of Physics, University of Oslo, P.O. Box 1048, Blindern, N-0316 Oslo, Norway

Received 6 June 2007; accepted 17 September 2007

Abstract

The results are presented of an electron magnetic resonance analysis at 110 K of radiation-induced defects in sucrose single crystals X-irradiated at room temperature, yielding a total of nine ^{1}H hyperfine coupling tensors assigned to three different radical species. Comparisons are made with results previously reported in the literature. By means of electron paramagnetic resonance and electron nuclear double resonance temperature variation scans, most of the discrepancies between the present 110 K study and a previous 295 K study by Sagstuen and co-workers are shown to originate from the temperature dependence of proton relaxation times and hyperfine coupling constants. Finally, radical models previously suggested in the literature are convincingly refuted by means of quantum chemical density functional theory calculations.

Keywords: EPR; ENDOR; DFT; Hyperfine coupling; Sucrose; Radiation; Temperature dependence

1. Introduction

The (in particular oxidative) radiation chemistry of saccharides has been the subject of intensive research the last decades for a number of reasons. Firstly, little is still known with certainty about the nature and reactions of radicals induced by direct radiation effects in the deoxyribose sugar of DNA and their roles with respect to important DNA damage processes [1,2]. Due to the complex nature of DNA, studying smaller model systems bearing key features similar to the DNA components has proven useful for gaining insight in these radiation-induced processes. In this context, saccharide single crystals are suitable systems for modeling the direct effects of ionizing radiation on the deoxyribose sugar unit in DNA.

Secondly, understanding the nature of radiation-induced defects in sugar compounds is important for radiation dosimetry purposes and for the detection and characterisation of irradiated foodstuffs. Sucrose (or table sugar) is of particular interest for nuclear emergency dosimetry because of its widespread use, its radiation sensitivity, the stability of the induced radicals [3,4], and its linear dose response up to 10^4 Gy [5]. More recent studies suggest sucrose to possibly be one of the best, universal materials for EPR (electron paramagnetic resonance)- and/or UV-dosimetry in the region 0.44–160 kGy [6,7].

Considerable efforts have been made to work out a comprehensive scheme of the radiation-induced radical chemistry of saccharides. Although a substantial number of sugars has been studied intensively and in great detail by means of EPR (electron paramagnetic resonance), ENDOR (electron nuclear

* Corresponding author. Tel.: +32 92644352; fax: +32 92644996.
E-mail addresses: hendrik.decooman@UGent.be (H. De Cooman), ewald.pauwels@ugent.be (E. Pauwels), henk.vrielinck@ugent.be (H. Vrielinck), annadimitrovabg@yahoo.com (A. Dimitrova), ndyepr@ic.bas.bg (N. Yordanov), einar.sagstuen@fys.uio.no (E. Sagstuen), michel.waroquier@ugent.be (M. Waroquier), Freddy.callens@ugent.be (F. Callens).

1386-1425/$ – see front matter © 2007 Elsevier B.V. All rights reserved.
doi:10.1016/j.saa.2007.09.033

double resonance) and EIE (endor-induced EPR) (e.g. sucrose [8–14], glucose-1-phosphate [15], methyl-α-D-glucopyranoside [16], α-D-glucopyranoside [17], β-D-fructose [18,19], rhamnose [20–25], trehalose [8,26,27]), the structures of the radiation-induced radicals could often not be unambiguously identified. Unravelling the detailed formation mechanism of the radicals is even more challenging, even if some more general mechanisms have emerged to be commonly operative from these studies.

In the past few years however, EMR (electron magnetic resonance) experimentalists have adopted a new tool to aid in solving these problems: density functional theory (DFT) quantum chemical calculations. Comparison of experimentally obtained EMR results with parameters calculated for a certain radical structure using DFT, may provide arguments for either rejection or validation of a proposed radical model. The energetics and feasibility of certain chemical reactions taking place can also, to some extent, be assessed by means of DFT. Due to the considerable increase in computer power and the availability of more accurate density functionals over the past few years, DFT calculations have evolved into a powerful tool for clarifying, interpreting and explaining experimental results. This synergy was nicely illustrated by e.g. the recent work of Vanhaelewyn and co-workers [19,28]. As a consequence, a renewed interest in the radiation-induced radical processes of saccharides has arisen and experimental results from the last few decades are re-investigated in search for new or more detailed radical models. An example is the computational study on rhamnose done by Pauwels and co-workers [29].

In the case of the disaccharide sucrose (see chemical structure in Fig. 1), the experimental results for RT (room temperature) radiation-induced defects in single crystals reported in literature, as obtained at different temperatures, are in disagreement at several points. This lack of reliable experimental data impedes the interpretation of the available data in terms of credible radical structures. In order to clear up this matter, a new EMR study at 110 K was undertaken in the present work and the role of the measuring temperature was carefully investigated by means of EPR and ENDOR temperature scans: for a number of specific orientations, spectra were recorded at temperatures between 20 K and RT. Careful and detailed comparisons are made with the most relevant literature results [11,13]. In addition, DFT calculations on the so far best radical models proposed in literature [11] are presented.

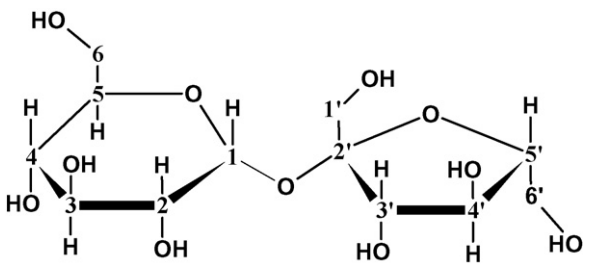

Fig. 1. The chemical structure of the sucrose molecule with the atomic numbering used in the present work.

2. Results reported in literature

Radiation-induced defects in sucrose have been investigated by means of EMR measurements at different temperatures (for both irradiation and measurements) in the past by a number of research groups [8–14]. After irradiation of sucrose single crystals at RT, composite EPR spectra are observed [8,11,13,14] at conventional microwave frequencies (X- and Q-band). This composite nature, in combination with the fairly small g-anisotropy of all involved radicals, impedes any analysis by means of EPR alone.

A first breakthrough was achieved by Sagstuen et al. [11]: RT EPR and ENDOR measurements were performed using sucrose single crystals X-irradiated at RT. Their analysis allowed for the determination of five proton hyperfine coupling tensors that were assigned to two different radicals. For one of these species these authors managed to extract a fairly precise g-tensor from Q-band measurements. They also used these data to propose radical structure models for the two species.

In 2000, a new EMR study on sucrose single crystals was published by Vanhaelewyn et al. [13]: their analysis of EPR, ENDOR and EIE measurements at 60 K using RT irradiated single crystals yielded altogether nine proton hyperfine coupling tensors, assigned to a total of three radicals. Two of these radicals were very similar, but clearly distinguishable. The number and characteristics of the coupling tensors were clearly different from those reported in [11], although some tensors did seem to show some similarity.

A third important study was recently carried out by Georgieva et al. [14]. Multifrequency EPR measurements on sucrose powders at different temperatures, including RT, confirmed the presence of at least three different radicals. The spectrum simulation analyses carried out in this work corroborated the results reported in [13] and allowed for estimations of the g-tensors of these three radical species.

3. Experimental

Analytical grade sucrose was obtained from Aldrich (98%) and was used to grow single crystals from H_2O or D_2O solutions. Recrystallisation from D_2O was performed three times, implying that approximately 99% of the exchangeable protons were replaced by deuterium. The crystal structure of sucrose is known from X-ray [30,31] as well as neutron [32] diffraction analysis. The crystals are monoclinic with space group $P2_1$ and a unit cell contains two molecules ($Z=2$). The crystal parameters were determined to be $a=1.0868$ nm, $b=0.8710$ nm, $c=0.7761$ nm and $\beta=102.97°$, β being the angle between the $\langle a\rangle$- and $\langle c\rangle$-axes. The a^*bc system ($\langle a^*\rangle$ being orthogonal to both $\langle b\rangle$ and $\langle c\rangle$) was chosen as orthogonal reference frame in this work, in analogy with previous publications. Due to the monoclinic symmetry combined with $Z=2$, the only allowed symmetry operation to be applied on the eigenvector matrices in this reference frame is a twofold rotation around $\langle b\rangle$ (being equivalent to changing the signs of all the eigenvector $\langle a\rangle$- and $\langle c\rangle$-components simultaneously), next to, of course, the inversion symmetry operation that is always present in case of EMR measurements. For a cer-

tain direction vector, the polar coordinates θ and φ are defined in the current work as the angles measured from the positive z-axis (=$\langle c \rangle$-axis) to the vector and the angle measured from the positive x-axis (=$\langle a^* \rangle$-axis) to the projection of the vector in the xy-plane (=a^*b-plane), respectively.

The single crystal samples used for the temperature scans were X-irradiated at RT to doses of 60–90 kGy using a Philips chromium-anode X-ray tube operated at 60 kV and 40 mA. They were then mounted to a goniometer head. For alignment of the direct crystal axes $\langle a \rangle$, $\langle b \rangle$ and $\langle c \rangle$ parallel to the rotation axis, the goniometer was put in a Weissenberg X-ray diffraction camera and oscillation diagrams were used. For determining the orientation of the rotation axis of the skewed plane, the goniometer was placed in a Bruker D8 Discover X-ray diffraction machine and stereographic projections were recorded for several crystallographic planes. With these methods, an accuracy of 0.5° and 2°, respectively is obtained. The crystals were then transferred from the goniometer head to a quartz crystal holder for EPR/ENDOR measurements with a minimal loss of alignment. EPR, ENDOR and EIE spectra were recorded at X-band (9.5 GHz) on a Bruker ESP300E spectrometer with an ESP353 ENDOR-Triple extension (Ghent) or on a Bruker Elexsys 560 spectrometer (Oslo) and at Q-band (34 GHz) on a Bruker ElexSys E500 spectrometer (Ghent). The spectrometers are equipped with Oxford flow cryostats, ESR910 (2–300 K), ESR900 (4–300 K) and CF935 (4.2–300 K), respectively.

The program MAGRES [33,34] was used to derive the hyperfine coupling tensors from the ENDOR data. A six-parameter linear regression routine generates these tensors from the polar angles θ and φ of the rotation axes, the measurement angle α (in the plane of rotation), and the corresponding measured ENDOR frequencies. Further refinements consisting of additional small variations of a total of 12 angles (the two polar angles for each of the rotation axes and the in-plane rotation starting angle for each plane) were made, using a nonlinear refinement procedure converging to a minimal root mean square (rms) value for the complete data set.

As for the temperature scans, in each instance the sample was first cooled to 20 K and then both EPR and ENDOR spectra were recorded at a number of temperatures while gradually warming up the sample to RT. In order to guarantee thermal stabilisation of the sample at each temperature setting, the spectra were recorded several minutes after the temperature displayed by the temperature controller had stabilised. Using this method and in the probed temperature range, the recorded temperature is expected not to differ more than 5 K from the actual specimen temperature.

The details on the computational procedures are presented together with the results of the DFT calculations.

4. Results and discussion

4.1. EPR, ENDOR and EIE at 110 K

In Fig. 2, a typical X-band 110 K EPR spectrum of sucrose irradiated at RT is shown. At this orientation of the magnetic field the composite character of the resonance is apparent from the significant asymmetry of the spectrum. At other orientations, a spectrum resembling a doublet of triplets is observed, as seen in Fig. 7 and as also reported in previous publications [8,11,13].

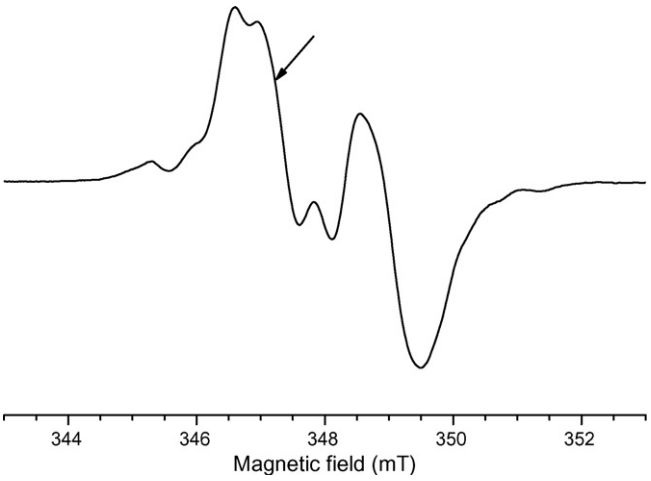

Fig. 2. X-band EPR spectrum at 110 K for RT X-irradiated sucrose crystals. The magnetic field was perpendicular to $\langle b \rangle$, 16° from $\langle a^* \rangle$ and 61° from $\langle c^* \rangle$; the microwave frequency was 9.748 GHz. The arrow marks the magnetic field at which the ENDOR spectrum of Fig. 3 was recorded.

Fig. 3 shows the corresponding ENDOR spectrum. This is one of the few orientations of the crystal in the external magnetic field for which the ENDOR lines in the generally crowded lower frequency range (18–25 MHz) are fairly well resolved. The ENDOR lines for which the analysis was successful and corresponding hyperfine coupling tensors were determined have been labelled in Fig. 3 in accordance with the labelling scheme in Table 1.

ENDOR measurements were performed at one or two magnetic field positions in the EPR spectrum in 5° steps over 130°

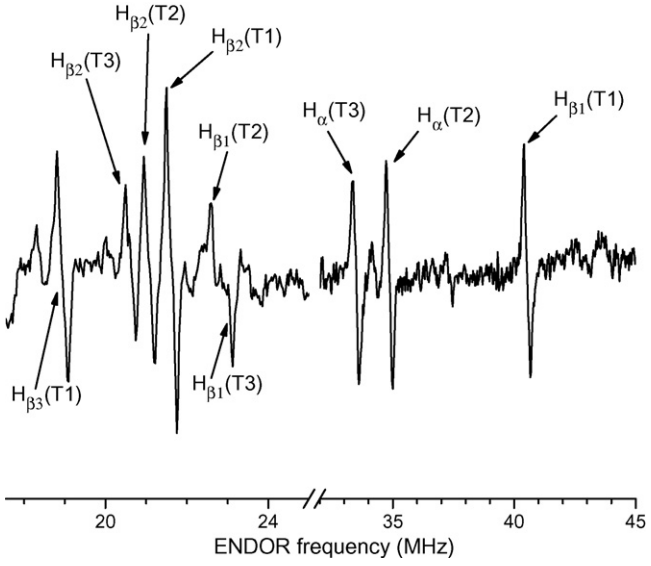

Fig. 3. X-band ENDOR spectrum at 110 K for RT X-irradiated sucrose. The magnetic field was perpendicular to $\langle b \rangle$, 16° from $\langle a^* \rangle$ and 61° from $\langle c^* \rangle$; the magnetic field was 347.2 mT. The ENDOR lines of the ^{1}H hyperfine interactions for which a tensor could be determined are marked using the labelling scheme of Table 1.

Table 1
Proton hyperfine coupling tensors (in MHz) of radicals T1, T2 and T3 in RT X-irradiated sucrose single crystals, measured at 110 K

Radical	Proton type	Isotropic values	Anisotropic values	Eigenvectors		
				a^*	b	c
T1	$H_{\beta 1}$	46.80	−3.99	0.616	0.121	−0.778
			−2.38	0.072	0.975	0.209
			6.37	0.784	−0.185	0.592
	$H_{\beta 2}$	15.88	−2.69	0.106	0.825	0.555
			−2.31	0.989	−0.144	0.025
			5.00	0.101	0.546	−0.832
	$^{A}H_{\beta 3}$	−11.07	−6.50	0.707	−0.245	−0.664
			−3.69	0.383	0.921	0.068
			10.19	0.595	−0.302	0.745
	$^{B}H_{\beta 3}$	−11.20	−8.00	0.602	−0.558	−0.572
			−0.59	0.580	0.797	−0.167
			8.59	0.549	−0.231	0.803
T2	H_{α}	−38.69	−19.66	0.424	−0.163	−0.891
			−2.11	0.886	0.280	0.371
			21.77	0.189	−0.946	0.263
	$H_{\beta 1}$	16.37	−2.32	0.869	−0.355	−0.344
			−1.72	−0.209	0.368	−0.906
			4.04	0.448	0.860	0.246
	$H_{\beta 2}$	13.68	−3.09	0.718	−0.650	0.248
			−2.17	0.638	0.473	−0.608
			5.26	0.278	0.595	0.754
T3	H_{α}	−35.81	−18.98	0.584	−0.184	−0.790
			−2.11	0.755	0.481	0.446
			21.09	0.298	−0.857	0.420
	$H_{\beta 1}$	16.42	−2.10	0.840	−0.541	−0.034
			−1.77	0.178	0.334	−0.926
			3.87	0.512	0.772	0.377
	$H_{\beta 2}$	12.24	−3.62	0.528	−0.822	0.214
			−2.12	0.804	0.402	−0.439
			5.74	0.275	0.403	0.873

The tensors were fitted using ENDOR angular variation plots in a total of four planes: three planes constituted by the direct crystal axes (Figs. 4 and 5) and a skewed plane (Fig. 6). For the $H_{\beta 3}$(T1) coupling, two possible alternatives are presented, $^{A}H_{\beta 3}$ being favoured by the fitting procedures over $^{B}H_{\beta 3}$. The assignment of the couplings to a total of three radical species was based on EIE measurements (Fig. 7).

(planes perpendicular to $\langle a \rangle$ and $\langle c \rangle$) or 180° (plane perpendicular to $\langle b \rangle$), or in 10° steps over 180° (skewed plane). The ENDOR line angular variation plots in the four experimental rotation planes are shown as points in Figs. 4–6. These data allowed for the determination of a total of nine ^{1}H hyperfine coupling tensors. Using only data points in the three planes perpendicular to the direct crystal axes (Figs. 4 and 5), two essentially different tensors were found fitting the data equally well for each of the ^{1}H hyperfine couplings. For most of the couplings it was not possible to reject with certainty either one of the two possibilities based on empirical arguments alone. Therefore, measurements were performed in a fourth, skewed plane (Fig. 6). For most couplings, this fourth plane did allow for the determination of the correct tensor with certainty. However, as the strong overlap of ENDOR lines allowed for only a few data points to be attributed to the $H_{\beta 3}$(T1) interaction, unambiguous differentiation of the obtained tensors for this coupling was not achieved, although one tensor seemed to be favoured (Fig. 6 and below).

The complete set of tensors finally arrived at are shown in Table 1. For the $H_{\beta 3}$(T1) coupling, both possibilities are listed, $^{A}H_{\beta 3}$(T1) being favoured over $^{B}H_{\beta 3}$(T1). The expected angular variations of the ENDOR lines calculated from these tensors are shown as solid lines in Figs. 4 and 5 (and for some also in Fig. 6). As discussed in Section 3, slight misorientations (<1.5°) of the crystals used for the recording of spectra were included in the final analysis. With exception of the $H_{\beta 3}$(T1) coupling, a minimum of 10 data points per data set – corresponding to a single-line ENDOR angular variation in a certain plane and belonging to one certain crystal site – was included in the fitting. The spectra recorded using partially deuterated samples only differed from their non-deuterated counterparts in the distant proton region (13–17 MHz), implying that all nine interactions in Table 1 arise from non-exchangeable protons and are thus carbon-bound.

EIE measurements in X- as well as Q-band allowed for unambiguous attribution of the tensors to three different radical species, as indicated in Table 1. X-band EIE spectra of the three radicals are shown together with the EPR spectrum for a particular orientation in Fig. 7. For the EIE based assignment of the ^{1}H couplings to a certain radical, four different orientations were thoroughly probed at X-band, as well as two orientations at Q-band. In the Q-band spectra, radicals T2 and T3 were significantly better separated, but the signal to noise ratio was considerably lower.

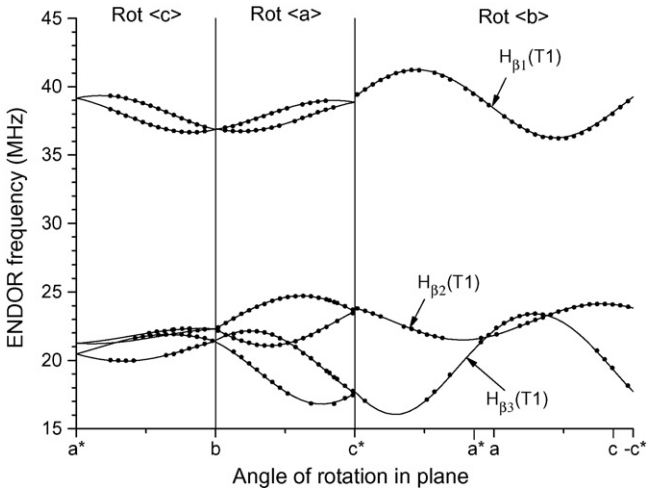

Fig. 4. X-band angular variation of the ENDOR transitions associated with radical T1 in RT X-irradiated sucrose, measured at 110 K. The labelling scheme of Table 1 is used. The spectra were normalised to a proton frequency of 14.480 MHz for the a^*b- and the bc^*-planes, and 14.760 MHz for the ac-plane. The dots represent experimentally determined ENDOR resonance positions, the full lines are the simulations of the ENDOR angular variations using the tensors in Table 1. The lack of connectivity between the planes at some points is due to a combination of slight tilting of the planes and different magnetic fields at which the ENDOR was recorded.

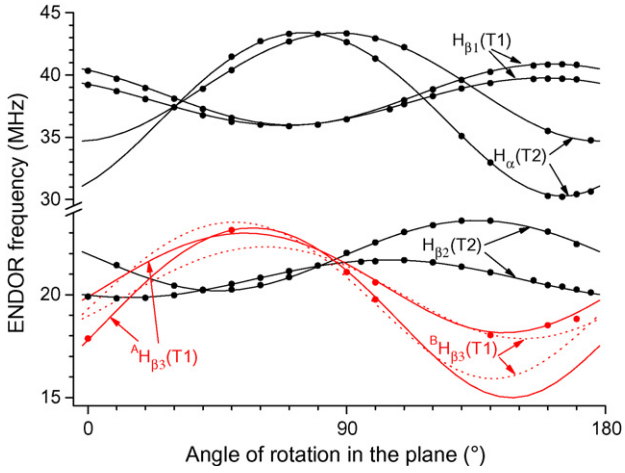

Fig. 6. X-band angular variation of the ENDOR transitions associated with some of the ^{1}H hyperfine couplings in RT X-irradiated sucrose, measured at 110 K. The polar angles of the plane are $\theta = 79.24°$ and $\varphi = 68.95°$ (reasonably close the ac-plane). The projections of $\langle a^* \rangle$, $\langle a \rangle$, $-\langle c \rangle$ and $-\langle c^* \rangle$ in this rotation plane are located at 20.4°, 33.8°, 105.7° and 118.2°, respectively. The dots represent experimentally determined ENDOR resonance positions, the full and dashed lines are the simulations of the ENDOR angular variations using the tensors in Table 1. The spectra were normalised to a proton frequency of 14.480 MHz. The labelling scheme of Table 1 is used.

For radical T1, the largest hyperfine coupling, $H_{\beta1}$(T1), exhibits the typical characteristics of an interaction with a carbon-bound β-proton [35] (Table 1). The $H_{\beta2}$(T1) tensor has anisotropic elements similar to those of $H_{\beta1}$(T1). However, the isotropic component is substantially smaller and the coupling may be due to a β- as well as a γ-proton interaction. As discussed above, there is still some uncertainty left with respect to the tensor of the $H_{\beta3}$(T1) coupling. The anisotropic part of tensor $^{A}H_{\beta3}$(T1), favoured by the data points in the fourth plane, roughly exhibits the axial symmetry characteristic of an interaction with a β-proton. In order to obtain the typical ($-b$, $-b$, $+2b$) anisotropy, with $b > 0$, the isotropic component has to be chosen negative, which is atypical for β-proton interactions. The other possible but slightly disfavoured tensor shape, $^{B}H_{\beta3}$(T1), is essentially different and exhibits the symmetry of an α-proton interaction. As sufficient data for further discriminating between

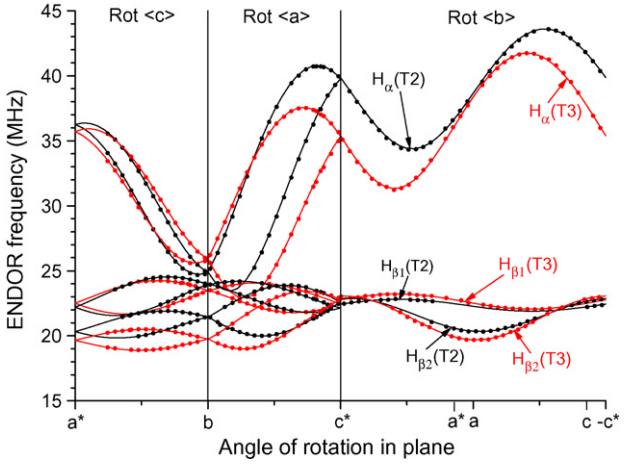

Fig. 5. X-band angular variation of the ENDOR transitions associated with radicals T2 and T3 in RT X-irradiated sucrose, measured at 110 K. The labelling scheme of Table 1 is used. The spectra were normalised to a proton frequency of 14.480 MHz for the a^*b- and the bc^*-planes, and 14.760 MHz for the ac-plane. The dots represent experimentally determined ENDOR resonance positions, the full lines are the simulations of the ENDOR angular variations using the tensors in Table 1. The lack of connectivity between the planes at some points is due to a combination of slight tilting of the planes and different magnetic fields at which the ENDOR was recorded.

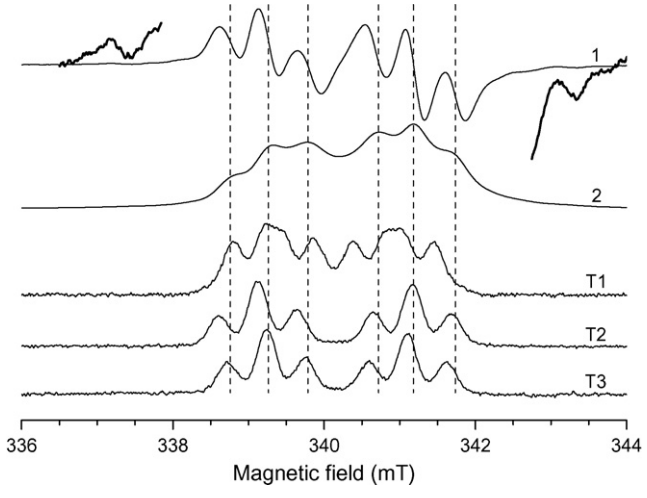

Fig. 7. *Top*: (1) first derivative X-band EPR spectrum of RT irradiated sucrose, measured at 110 K. The thick line was obtained by multiplying the intensity with a factor of 20. (2) Absorption EPR spectrum obtained by integrating spectrum 1. *Under*: absorption X-band EIE spectra of the three main radicals (Table 1), all in non-derivative absorption mode. All spectra are normalised to a microwave frequency of 9.550 GHz. The magnetic field is oriented perpendicular to $\langle b \rangle$, at 118° from $\langle a \rangle$ and 15° from $\langle c \rangle$. The weak features at either side of the EPR spectrum show that at least one other radical species, fundamentally different from T1, T2 and T3 is present in RT irradiated sucrose.

these two alternatives are presently not available, this matter will not be addressed further here. Both alternatives are included in Table 1.

The hyperfine coupling tensors due to radical species T2 and T3 are very similar, strongly suggesting that T2 and T3 are two slightly different geometrical configurations of the same radical entity. Similar observations have been made in other saccharides such as fructose [19] and sorbose [28]. A possible explanation for the observations made in sucrose would be that one or more minor structural differences in the immediate molecular environment of the radical are causing these relatively small differences. As will be discussed below, it is very likely that other slightly different conformations of this radical entity are present, albeit in considerably lower concentrations.

Both T2 and T3 are characterised by three ^{1}H hyperfine interactions. The largest coupling is clearly due to an α-proton interaction. The spin density on an α-proton can be estimated using either the isotropic (McConnell relation [36], Eq. (1)) or the anisotropic values (Gordy–Bernhard relation [37], Eq. (2)) of the hyperfine tensor:

$$a_{\alpha,\mathrm{iso}} = Q^{\alpha}_{\mathrm{iso}}\rho_{\pi} \quad (1)$$

$$b_{+,\mathrm{dip}} = Q^{\mathrm{H}}_{\alpha,\mathrm{dip}}\rho_{\pi} \quad (2)$$

where $a_{\alpha,\mathrm{iso}}$ is the isotropic component, $b_{+,\mathrm{dip}}$ is the most positive dipolar component, ρ_{π} is the unpaired spin density localised on the carbon in the molecular π-orbital and $Q^{\alpha}_{\mathrm{iso}}$ and $Q^{\mathrm{H}}_{\alpha,\mathrm{dip}}$ are empirical "constants", dependent to some extent on the nature of the radical fragment. For $Q^{\alpha}_{\mathrm{iso}}$ a value of −72 MHz will be assumed [38] and for $Q^{\mathrm{H}}_{\alpha,\mathrm{dip}}$, the value of 38.7 MHz, as proposed by Bernhard [39]. Eqs. (1) and (2) both yield unpaired electron densities of 0.50–0.55 for both radicals, indicating (i) that about 50% of the unpaired spin density is delocalised on a neighbouring oxygen or carbon and (ii) that the spin centres are essentially planar [39]. Sagstuen et al. [11] made similar observations and as a possible explanation the presence of a neighbouring carbonyl group was suggested. As the $H_{\beta 1}$ and $H_{\beta 2}$ tensors of radicals T2 and T3 have relatively small isotropic components, the possibility for these tensors to be due to couplings to β- as well as γ-protons should be considered.

A careful analysis of the ENDOR spectra revealed that the T2 and T3 signals in all rotation planes are closely accompanied by a number of considerably less intense resonance lines, some of which can be seen in Fig. 3. This was also reported by Vanhaelewyn et al. [13]. This indicates that other radicals, differing only slightly in geometry from the T2/T3 radicals, are present in RT irradiated sucrose. Yet other weak ENDOR lines clearly indicate the existence of at least one other radical species fundamentally different from the three characterised in Table 1. The presence of such a radical can also be deduced from comparison of the EIE spectra of radicals T1, T2 and T3 with the experimental EPR spectrum (Fig. 7).

4.2. EPR and ENDOR temperature scans

As indicated in Section 1, there are important qualitative and quantitative differences, between the 60 K results reported by Vanhaelewyn et al. [13] and the RT results reported by Sagstuen et al. [11]. Moreover, the data presented in the current work were acquired at 110 K, a somewhat intermediate temperature. The study performed by Georgieva et al. [14] also covers a wide range of temperatures. In order to elucidate the effects of the measuring temperature on the ENDOR spectra and hence on the proton hyperfine coupling tensors extracted, a series of EPR and ENDOR temperature scans was performed on RT X-irradiated sucrose single crystals at different orientations in the magnetic field.

The high frequency EPR study by Georgieva et al. [14] provides convincing proof that three different radicals are present after X-irradiation at RT, and not two as suggested by Sagstuen et al. [11]. Since the samples in all studies were irradiated at RT, variations of the signal upon lowering the temperature followed by rewarming to RT, should be reversible. Therefore, one expects the same three radicals to be present at 60 K and at RT, possibly with some reversible geometrical alterations.

Figs. 8–11 show EPR (Fig. 8) and ENDOR (Figs. 9–11) temperature scans for both the weakly and the strongly coupled proton frequency ranges and at two different orientations of the crystal in the magnetic field. From Fig. 8 it is apparent that the Q-band EPR spectrum is only slightly temperature dependent in the region 60–300 K. In particular from 190 K onwards, a gradual shift of the resonance lines towards higher fields is apparent, without the overall pattern of the EPR signal being altered. Similar scans at other orientations all strongly suggest that there are in fact no fundamental differences between the radicals present at 60 K and at RT. As will be apparent from the discussion below, the magnetic field shifts cannot be explained solely by virtue of the variation of the hyperfine couplings with temperature. Therefore, a slight temperature dependence of the g-tensors accompanying the radical geometry changes seems to be the most plausible explanation. This matter was not further investigated.

Figs. 9 and 10 lead to the following conclusions with respect to the temperature dependence of the hyperfine interactions in

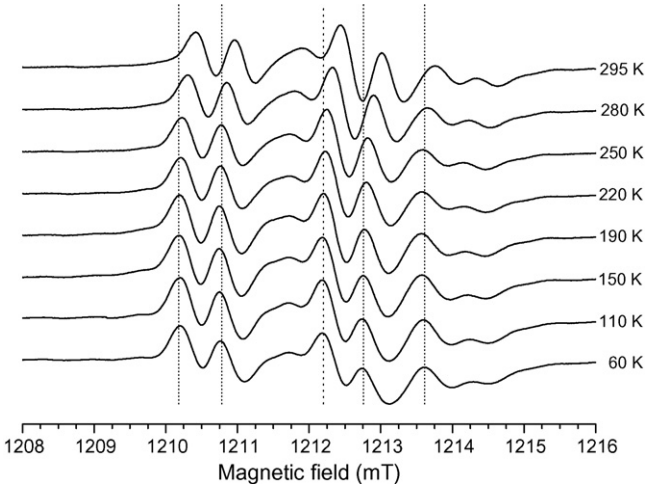

Fig. 8. Q-band EPR temperature scan for RT irradiated sucrose. The magnetic field was perpendicular to ⟨*b*⟩, 25° from ⟨*a**⟩ and 52° from ⟨*c**⟩. All spectra were normalised to a microwave frequency of 34.000 GHz.

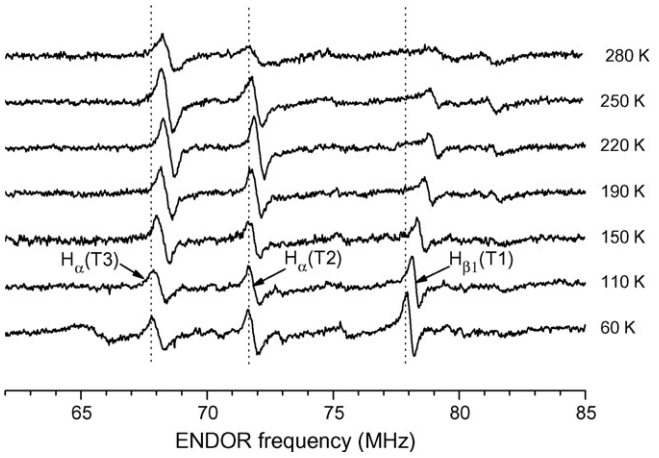

Fig. 9. Q-band ENDOR temperature scan for the strongly coupled frequency region. The magnetic field was perpendicular to the ⟨*b*⟩, 25° from ⟨*a**⟩ and 52° from ⟨*c**⟩. All spectra were 'normalised' to a magnetic field of 1214.29 mT using the proton frequencies as a reference. The labelling scheme of Table 1 is used.

the strongly coupled proton frequency range. These conclusions are supported by temperature scans at several other orientations not shown here:

(i) At most orientations the signal of the $H_{\beta1}$(T1) resonance line gradually loses intensity with increasing temperature from 150 K and has almost completely disappeared at RT. This signal also shifts to somewhat higher frequencies with increasing temperature, with a difference between the signal positions at 60 K and at 280 K of typically 1–2 MHz. This effect is particularly well observable in Fig. 10.

(ii) At most orientations the H_α(T2) resonance line is significantly reduced in intensity as compared to the H_α(T3) line when the temperature increases from 250 to 280 K. These two resonance line positions are only very slightly temperature dependent. It should be noted that the merging of the H_α(T2) and H_α(T3) signals at the orientation of Fig. 10 is solely a coincidence. The practical fact remains that at RT, only one resonance line due to the H_α(T2) coupling is seen with reasonable intensity in this frequency range.

(iii) In Fig. 10, the two weak resonance lines still accompanying the H_α(T2) and H_α(T3) signals at 160 K have disappeared, or possibly merged with their more intense neighbouring signals, at 190 K. These are examples of signals very likely arising from radical structures with geometrical configurations slightly different from those for the T2/T3 radicals (cf. Section 4.1).

As the frequency range for the weakly coupled protons is extremely crowded, attempts to derive detailed information for the ENDOR transitions in this frequency range were virtually unsuccessful. Fig. 11 shows one of the most illustrative scans obtained. Most resonance lines are subject to small frequency shifts as the temperature increases from 20 to 160 K. From 160 K upwards, some more clear changes are observed and most signals become reduced in intensity. At 280 K, only one resonance line with appreciable intensity is left. This line seems to be a superposition of the shifted and merged $H_{\beta1}$(T2) and $H_{\beta1}$(T3) resonance lines. The $H_{\beta2}$(T2), $H_{\beta2}$(T3) and $H_{\beta2}$(T1) lines are also present at 280 K, but with almost negligible intensity. However, it should be noted that the relative intensities of the resonance lines at RT are angular dependent and that, in general, the T2 and T3 radical resonance lines do not merge. Finally, from the available data it was not possible to draw any conclusions concerning the temperature dependence of the $H_{\beta3}$(T1) signal.

In summary, the differences between the EPR and ENDOR spectra at 60 K and at 110 K are practically negligible. Furthermore, a number of ENDOR lines show small frequency shifts and eventually disappear as the temperature is raised to RT. As the EPR spectrum is only slightly temperature dependent, the apparent disappearance of some of the ENDOR lines is proba-

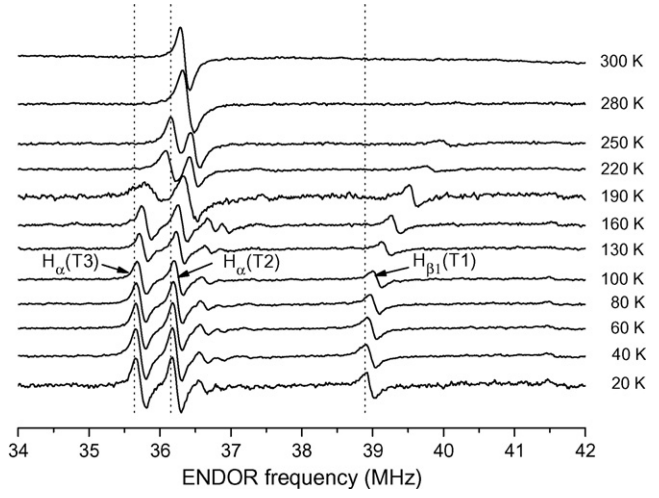

Fig. 10. X-band ENDOR temperature scan for the strongly coupled frequency region. The magnetic field was parallel to ⟨*a**⟩. All spectra were normalised to a magnetic field of 339.33 mT using the proton frequencies as a reference. The labelling scheme of Table 1 is used.

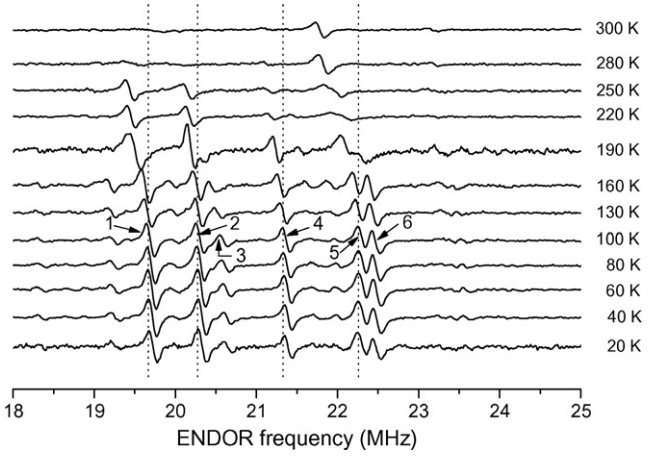

Fig. 11. X-band ENDOR temperature scan for the weakly coupled frequency region. The magnetic field was parallel to ⟨*a**⟩. All spectra were normalised to a magnetic field of 339.33 mT using the proton frequencies as a reference. Using the labelling scheme of Table 1, numbers 1–6 correspond to following interactions: 1 = $H_{\beta2}$(T3), 2 = $H_{\beta2}$(T2), 3 = $H_{\beta3}$(T1), 4 = $H_{\beta2}$(T1), 5 = $H_{\beta1}$(T2) and 6 = $H_{\beta1}$(T3).

bly due to temperature dependence of nuclear relaxation rates influencing the saturation behaviour of the ENDOR transitions. It is concluded that the same radicals are present and detected at RT and at 60/110 K with only some minor reversible changes in the radical geometry and/or spin density distributions. Thus, a fair agreement between the proton hyperfine coupling tensors acquired at different temperatures is to be expected.

4.3. Comparison with single crystal data obtained at other temperatures

In Tables 2 and 3 the tensors reported by Sagstuen et al. [11] (RT) and by Vanhaelewyn et al. [13] (60 K) are listed. Some sign changes have been applied in both tables, for principal values as well as for some eigenvector matrix elements. A number of these changes are actual corrections to the published tensors, and were made after consulting the authors concerned. Other changes are allowed symmetry operations applied with the aim of facilitating comparison with the tensors presented in the current work (Table 1). For the reader's convenience, the original radical and tensor labels are used.

Firstly the tensors obtained at 60 K ([13], Table 3) will be compared with those obtained at 110 K (current work, Table 1). It is instantly clear that radicals S1, S2 and S3 correspond to radicals T1, T2 and T3, respectively. Not only is the match for the isotropic components excellent for all interactions, the anisotropic couplings are also in the same range. However, the symmetry of the anisotropic parts shows some clear differences, especially for the six hyperfine couplings with smaller isotropic components. Moreover, although the eigenvector matrices do not seem to be entirely dissimilar, careful comparison reveals that the directional agreement is poor.

These quantitative discrepancies are far too large to be the result of a difference in measuring temperature, as is clear from the temperature scans discussed above. One possible explanation could be the fact that Vanhaelewyn et al. [13] only used two planes of data points to extract the proton hyperfine coupling tensors from, whereas in the current study four planes were used. When the symmetry is lower than axial, three independent planes of data are in principle required for an accurate and unambiguous fitting. In practice, even a fourth, skewed plane is often a necessity, as was the case in the study presented in the current work. Based on the above arguments and supported by the discussion below, it is concluded that the tensors obtained in the present study at 110 K (Table 1) are the most accurate set of EPR parameters for the three main radical species in RT irradiated sucrose. With this new and more accurate data available, a re-evaluation of the g-tensor analysis reported in [14] may appear necessary.

When comparing the 110 K data set (current work, Table 1) and the RT one ([11], Table 2), a number of qualitative differences is immediately obvious. First of all, the $H_{\beta1}$(T1) coupling, very prominent in the ENDOR spectra recorded at 110 K (Fig. 3), is not reported in [11]. This is readily explained by means of the ENDOR temperature scans (Figs. 9 and 10), where the corresponding ENDOR line was clearly shown to have lost its intensity almost completely at RT. Secondly, only two radicals are reported in [11], whereas three radicals are observed at 110 K. The temperature scans again provide an explanation as Figs. 9 and 10 clearly show that the H_{α}(T2) resonance line is substantially reduced in intensity at RT, as compared to the H_{α}(T3) signal. Moreover, at a number of orientations this already (very) weak signal accidentally merges with the H_{α}(T3) resonance line, leaving it undetectable. Although no final conclusions could be arrived at with regard to the temperature dependency of the smaller couplings (Fig. 11), it is certainly possible that also the $H_{\beta1}$(T2) and $H_{\beta2}$(T2) signals lose intensity and/or accidentally merge with the $H_{\beta1}$(T3) and $H_{\beta2}$(T3) signals. Sagstuen et al. [11] did report on the presence of yet another ENDOR line, which they believed to be an α-proton hyperfine interaction.

Table 2
Proton hyperfine coupling tensors (in MHz) reported by Sagstuen et al. [11] of radicals R1 and R2 in RT X-irradiated sucrose single crystals, measured at RT

Radical	Proton type	Isotropic values	Anisotropic values	Eigenvectors			Comparison with tensors of Table 1			
				a^*	b	c	Tensor	ψ (°)	Tensor	ψ (°)
R1	H_{α}	−37.67	−20.09	0.548	−0.175	−0.818	H_{α}(T2)	8.2	H_{α}(T3)	2.6
			−1.49	0.793	0.421	0.441		10.4		3.8
			21.57	0.267	−0.890	0.369		8.3		4.1
	$H_{\beta1}$	15.14	−2.15	0.856	−0.517	−0.023	$H_{\beta1}$(T2)	20.7	$H_{\beta1}$(T3)	1.1
			−1.72	0.183	0.261	−0.950		23.3		2.5
			3.88	0.484	0.816	0.317		5.0		4.3
	$H_{\beta2}$	12.43	−3.39	0.625	−0.746	0.231	$H_{\beta2}$(T2)	7.6	$H_{\beta2}$(T3)	7.0
			−2.15	0.726	0.447	−0.523		7.1		7.0
			5.54	0.287	0.495	0.820		6.9		6.2
R2	$H_{\beta3}$	15.57	−2.89	0.227	0.802	0.552	$H_{\beta2}$(T1)	7.2		
			−2.30	0.971	−0.233	−0.061		7.0		
			5.18	0.080	0.550	−0.832		1.5		
	$H_{\beta4}$	18.57	−2.60	−0.127	−0.931	−0.343				
			−1.48	0.975	−0.054	−0.214				
			4.07	0.181	−0.362	0.915				

Some sign corrections and symmetry operations have been applied. At the right hand side, the angular deviations (ψ) with the corresponding eigenvectors of the tensors of Table 1 obtained at 110 K, are given.

Table 3
Proton hyperfine coupling tensors (in MHz) reported by Vanhaelewyn et al. [13] of radicals S1, S2 and S3 in RT X-irradiated sucrose single crystals, measured at 60 K

Radical	Proton type	Isotropic values	Anisotropic values	Eigenvectors		
				*a**	*b*	*c*
S1	H_{α}	46.4	−4.2	0.748	−0.348	0.565
			−2.5	0.427	0.904	−0.007
			6.7	−0.509	0.247	0.825
	$H_{\beta1}$	16.0	−2.5	−0.853	−0.255	0.455
			−0.2	0.253	−0.965	−0.066
			2.8	0.456	0.059	0.888
	$H_{\beta2}$	11.4	−9.0	−0.327	0.145	0.934
			2.5	0.165	−0.964	0.207
			6.4	0.930	0.222	0.292
S2	H_{α}	−38.9	−18.7	0.742	−0.034	0.669
			−0.6	−0.661	−0.200	0.723
			19.4	0.109	−0.979	−0.172
	$H_{\beta1}$	16.5	−2.7	−0.895	0.378	−0.238
			−0.9	−0.142	0.265	0.954
			3.6	0.424	0.887	−0.183
	$H_{\beta2}$	13.8	−3.7	−0.880	−0.465	0.028
			1.0	0.454	−0.874	−0.175
			2.8	0.106	−0.142	0.984
S3	H_{α}	−36.4	−17.5	0.869	0.005	0.494
			2.1	−0.467	−0.321	0.824
			15.4	0.163	−0.947	−0.276
	$H_{\beta1}$	16.5	−3.1	−0.846	0.459	−0.272
			0.0	−0.148	0.289	0.946
			3.0	0.513	0.840	−0.176
	$H_{\beta2}$	12.4	−4.1	−0.883	−0.467	0.045
			−0.4	0.454	−0.874	−0.174
			4.5	0.121	−0.133	0.984

Some sign corrections and symmetry operations have been applied.

The signal intensity was too weak, however, to allow for a full analysis.

Based on these observations one would thus expect radical R1 to correspond to radical T3 and radical R2 to radical T1. When comparing radicals R1 and T2/T3, a close correspondence in isotropy and anisotropy is observed for all three tensors, in particular when considering the different measuring temperatures. Based on these criteria, it is however not possible to distinguish with certainty between T2 and T3. In Table 2 an explicit comparison of the eigenvector directions is presented. In both cases the match is obvious, but a substantially better agreement emerges between the R1 and T3 radicals, especially in case of the $H_{\beta1}$(T2)/$H_{\beta1}$(T3) tensors. The temperature clearly does not have much influence on the tensors. These observations already confirm a part of the prediction made above.

The comparison of radicals R2 and T1 is less straightforward. The agreement between the $H_{\beta3}$(R2) and $H_{\beta2}$(T1) tensors is excellent on all accounts (Table 2), strongly suggesting that radical R2 does indeed correspond to radical T1. However, the $H_{\beta4}$(R2) and the $H_{\beta3}$(T1) tensors are completely different (for both possible tensor shapes of the $H_{\beta3}$(T1) coupling). For this interaction, no clear-cut information was obtained from the temperature scans. One possible explanation is that with increasing temperature, a substantial shift in unpaired electron density occurs, prompted by geometric alterations of the radical, in turn giving rise to either a β-coupling with significantly different characteristics, or even a coupling with another proton. Extended investigations would be necessary to resolve this matter.

4.4. DFT study on radical models proposed in literature

As described in Section 2, numerous studies have been performed in the past on RT radiation-induced defects in sucrose. However, only Sagstuen et al. [11] made some effort in searching for suitable radical models by taking into account the specific characteristics of all tensors. The radical structures they proposed as candidate models for the R1/T2/T3 radical are shown in Fig. 12 (structures III and IV in Sagstuen et al. [11]). In both cases a carbonyl group is positioned in a β-position to the carbon at which the main spin density is localised. The presence of this functional group was proposed to cause substantial delocalisation of the unpaired electron spin density onto the oxygen atom, which would result in isotropic and anisotropic components of the α-coupling to become considerably reduced, as is experimentally observed (Table 1). This would also account for the g-factor anisotropy being larger than for a typical carbon centred radical [11]. The assignment of these radical models was only tentative, however.

A first attempt at checking the validity of these models by means of DFT was made by Georgieva et al. [14]. That study

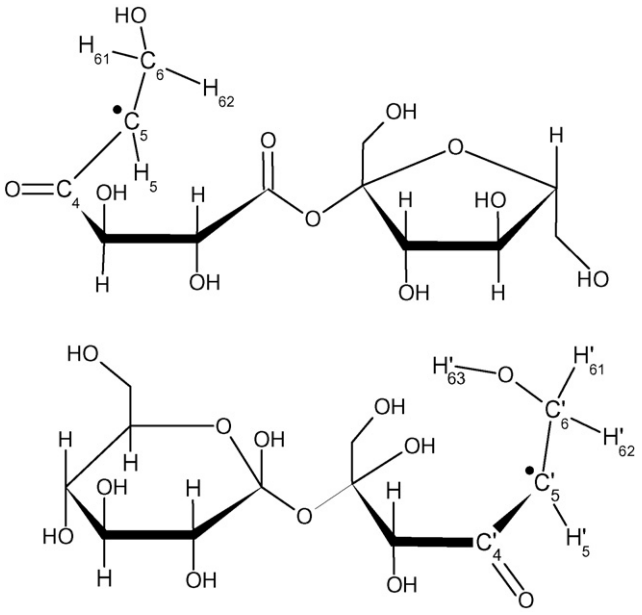

Fig. 12. Chemical structures of radical structures III (top) and IV (bottom) proposed by Sagstuen et al. [11] as possible models for the R1/T2/T3 radical in RT irradiated sucrose.

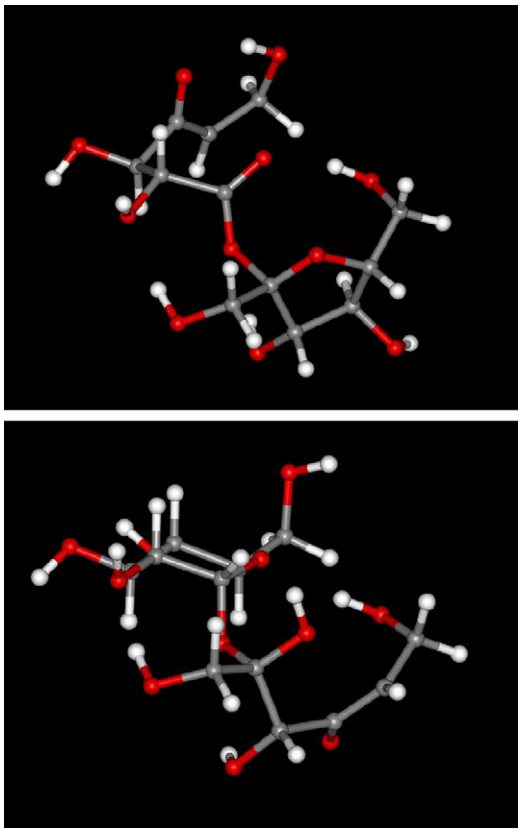

Fig. 13. 3D figures of radical structures III (top) and IV (bottom) (Fig. 12) after DFT geometry optimisation on a ⟨*ab*2*c*⟩ supercell in a periodical scheme.

points out some general tendencies for coupling sizes and, in this context, gives some indications as to which kind of radical models should be pursued for the T2/T3 radical. It did however not present any final conclusions on this issue.

For this reason, a more advanced DFT study was undertaken in the present work. As the crystalline environment can evidently be crucial for the geometry of the radical, especially in the case of broken ring structures, geometry optimisations should be performed in a theoretical methodology that appropriately accounts for this environment. In the literature, both cluster [19,29] and periodic [40] approaches have been successfully adopted to simulate free radical structures in the solid state. In a cluster approach, only part of the molecular environment is explicitly taken up in the calculations, whereas a periodic scheme exploits the translational symmetry of the crystal and hence, automatically and fully incorporates the lattice environment. The latter approach is in principle best suited as it offers the most complete description of a crystalline system and does not require the constraints that are usually imposed on the boundary molecules/atoms of a cluster. Therefore, a periodic approach was adopted in this work for all geometry optimisations. To ensure that the radical was well separated from its periodic images, an ⟨*ab*2*c*⟩ supercell was used, obtained by doubling the original crystal unit cell in the ⟨*c*⟩ direction. All calculations were performed with the CPMD software package [41], using a BP86 gradient-corrected density functional [42,43], together with a plane wave basis set (with a maximum kinetic energy of 25 Ry for the plane waves) and ultra-soft pseudopotentials of the Vanderbilt type [44]. No geometric restrictions were imposed on the atoms of the supercell.

The EPR properties of the free radical were subsequently calculated adopting a cluster scheme. A cluster was cut out of each periodically optimised structure such that it contained the radical and all (intact) molecules hydrogen bound to it (10 sucrose molecules in total). Hyperfine coupling tensors were calculated with the aid of the Gaussian 03 software suite [45], employing the B3LYP functional [46] and a 6-311G(d,p) basis set [47,48] for all atoms within the cluster. It has been shown [49] that incorporating the molecular environment in an EPR calculation can sometimes considerably improve its accuracy. In this respect, the proposed hybrid periodic/cluster scheme meets this demand at a sufficient level of theory [50].

The optimised radical structures are depicted in Fig. 13. The results of the EPR calculations on the optimised structures are presented in Table 4. As the α-tensors are often giving the most crucial information, these will be discussed first. The isotropic components of the α-proton couplings are indeed considerably reduced (as compared to 'normal' α-couplings [35]) but neither of the values obtained match the experimentally determined values for the T2 and T3 radicals (Table 1). Also, the calculated anisotropic coupling constants exceed the experimental values by about 50% in both cases. Although DFT calculations are known not to reproduce experimental values for isotropic couplings very accurately in some cases, the differences in anisotropy seem too big to be attributed to the inherent inaccuracy of DFT methods.

Using Eq. (2) (which is most reliable as the value of $Q^{H}_{\alpha,dip}$ is only slightly dependent on the radical geometry [39]), unpaired spin densities on the α-carbon of $\rho_\pi \approx 0.88$ and $\rho_\pi \approx 0.92$ are obtained for radical structures III and IV, respectively, which is

Table 4
Proton hyperfine coupling tensors for radical structures III and IV, obtained by means of cluster DFT calculations on radical structures acquired from periodic optimisations (Figs. 12 and 13)

Radical model	Proton	Isotropic values (MHz)	Anisotropic values (MHz)	Eigenvectors		
				*a**	*b*	*c*
III	H_5	−49.45	−31.48	−0.365	0.166	0.916
			−2.54	−0.330	0.897	−0.293
			34.02	0.871	0.409	0.273
	H_{61}	68.33	−4.41	0.599	0.248	0.761
			−2.53	−0.431	0.901	0.045
			6.94	0.675	0.355	−0.647
	H_{62}	4.82	−4.68	0.845	0.428	0.319
			−3.51	−0.302	0.877	−0.374
			8.19	−0.440	0.220	0.871
IV	H'_5	−30.50	−29.69	0.873	−0.294	−0.390
			−5.99	0.434	0.102	0.895
			35.68	0.223	0.950	−0.217
	H'_{61}	43.74	−4.46	0.172	0.814	−0.555
			−3.88	0.198	0.523	0.829
			8.33	0.965	−0.253	−0.071
	H'_{62}	98.80	−4.87	−0.388	0.776	−0.497
			−1.91	0.582	0.624	0.521
			6.78	0.714	−0.088	−0.694
	H'_{63}	10.70	−3.35	0.422	0.902	−0.088
			−1.91	0.769	−0.408	−0.491
			5.26	0.479	−0.139	0.867

surprisingly high. The Mulliken atomic spin densities reported by the Gaussian program on the α-carbon atoms are 0.84 and 0.78 for models III and IV, respectively, confirming these results on a qualitative level. Eq. (1), on the other hand, yields $\rho_\pi \approx 0.69$ and $\rho_\pi \approx 0.42$ for structures III and IV. Such differences normally indicate that the radical centres are significantly bent [37,39], thus prohibiting significant delocalisation of the unpaired spin onto the carbonyl group. The Mulliken atomic spin densities on the carbonyl group are 0.26 and 0.21 for models III and IV, respectively corroborating this reasoning. However, as the calculated radical geometries are known, the planarity can be readily assessed. For structure III, the dihedral angle C_4–C_5–C_6–H_5 (i.e. the angle between the C_4–C_5–C_6 plane and the C_5–C_6–H_5 plane) is 179.9°, for structure IV, a dihedral angle C'_4–C'_5–C'_6–H'_5 of 170.8° is found (Fig. 12). The almost perfect planarity for radical structure III (and, correspondingly, the surprisingly high actual spin density on the α-carbon) possibly suggests that the differences in calculated spin densities mentioned above are due to some other factor than bending of the radical centre. As this is of no importance for the goal of the present study, this was not further investigated.

It can be concluded that the general shapes of the α-tensors obtained by DFT calculations on radical structures III and IV do not bear much resemblance with the experimentally observed α-tensor shapes of radicals T2 and T3.

Some more results, suggesting that radical structures III and IV are not valid models, emerge from the DFT calculations (Table 4). Firstly, the isotropic components of the $H_{\beta 1}$ proton in model III and of both H_β protons in model IV are far too large as compared to the experimental values. Secondly, careful examinations show no match whatsoever between the calculated and experimentally determined eigenvectors for either of the couplings. Finally, the calculations on radical structure IV indicate that an appreciable coupling with the hydroxylproton H'_{63} (Fig. 12) should be observable. No such coupling was observed in the ENDOR spectra. Moreover, spectra recorded using partially deuterated samples clearly indicated that none of the major couplings are due to exchangeable protons.

5. Conclusion

The present study was undertaken to provide an understanding of the various differences in the experimental EMR as well as computational DFT data previously reported in the literature on RT radiation-induced radicals in single crystals of sucrose [11,13]. A new set of nine ^{1}H hyperfine coupling tensors was obtained from EMR measurements at 110 K. These were attributed to a total of three radical species as also was indicated in previous studies [13,14]. Good quantitative agreement was found with the data published by Sagstuen et al. [11] on most accounts and a qualitative agreement was found with the data by Vanhaelewyn et al. [13]. For radicals T2/T3, differences in measuring temperature cause only minor and reversible changes in the 20–295 K range. The T1 radical seems to be somewhat more temperature dependent, especially in the 250–295 K range. The data set presented in this work (Table 1) should be considered as the most accurate for the main RT radiation-induced radical species in sucrose in the 20–295 K temperature range with regard to radicals T2 and T3, and in the 20–250 K range – and possibly up to RT – with regard to radical T1. Some ambiguity concerning one of the smaller T1 hyperfine interactions still exists, however.

The results from DFT calculations performed on the radical structures proposed by Sagstuen et al. [11] strongly suggest that these structures are not suitable models for the T2/T3 radicals. Consequently, the molecular structures of all RT radiation-induced radicals in crystalline sucrose remain unknown.

References

[1] W.K. Pogozelski, T.D. Tullius, Chem. Rev. 98 (1998) 1089–1107.
[2] W.A. Bernhard, D.M. Close, in: A. Mozumdar, Y. Hatano (Eds.), Charged Particle and Photon Interactions with Matter Chemical, Physicochemical and Biological Consequences with Applications, Marcel Dekker, Inc., New York, 2004, pp. 431–470.
[3] T. Nakajima, Health Phys. 55 (1988) 951–955.
[4] T. Nakajima, Appl. Radiat. Isot. 46 (1995) 819–825.
[5] F. Americo, M. Silveira, O. Baffa, Appl. Radiat. Isot. 46 (1995) 827–830.
[6] N.D. Yordanov, V. Gancheva, E. Georgieva, Radiat. Chem. Phys. 65 (2002) 269–276.
[7] N.D. Yordanov, E. Georgieva, Spectrochim. Acta Part A 60 (2004) 1307–1314.
[8] A. Gräslund, G. Löfroth, Acta Chem. Scand. B 29 (1975) 475–482.
[9] E.E. Budzinski, W.R. Potter, G. Potienko, H.C. Box, J. Chem. Phys. 70 (1979) 5040–5044.
[10] H.C. Box, E.E. Budzinski, J. Chem. Phys. 79 (1983) 4142–4145.
[11] E. Sagstuen, A. Lund, O. Awaldelkartim, M. Lindgren, J. Westerling, J. Chem. Phys. 90 (1986) 5584–5588.
[12] H.C. Box, E.E. Budzinski, H.G. Freund, J. Chem. Phys. 93 (1) (1990) 55–57.
[13] G. Vanhaelewyn, J. Sadlo, F. Callens, W. Mondelaers, D. De Frenne, P. Matthys, Appl. Radiat. Isot. 52 (2000) 1221–1227.
[14] E.R. Georgieva, L. Pardi, G. Jeschke, D. Gatteschi, L. Sorace, N.D. Yordanov, Free Radic. Res. 40 (2006) 553–563.
[15] B. Bungum, E.O. Hole, E. Sagstuen, M. Lindgren, Radiat. Res. 139 (1994) 194–202.
[16] K.P. Madden, W.A. Bernhard, J. Phys. Chem. 84 (1980) 1712–1717.
[17] K.P. Madden, W.A. Bernhard, J. Phys. Chem. 86 (1982) 4033–4036.
[18] G. Vanhaelewyn, P. Lahorte, F. De Proft, W. Mondelaers, P. Geerlings, F. Callens, Phys. Chem. Chem. Phys. 3 (2001) 1709–1716.
[19] G. Vanhaelewyn, E. Pauwels, F. Callens, M. Waroquier, E. Sagstuen, P. Matthys, J. Phys. Chem. A 110 (2006) 2147–2156.
[20] P.O. Samskog, A. Lund, G. Nilsson, M.C.R. Symons, J. Chem. Phys. 73 (1980) 4862–4866.
[21] P.O. Samskog, A. Lund, Chem. Phys. Lett. 75 (1980) 525–527.
[22] P.O. Samskog, L.D. Kispert, A. Lund, J. Chem. Phys. 79 (1983) 635–638.
[23] E.E. Budzinski, H.C. Box, J. Chem. Phys. 82 (1985) 3487–3490.
[24] H.C. Box, E.E. Budzinski, H.G. Freund, Radiat. Res. 121 (1990) 262–266.
[25] E. Sagstuen, M. Lindgren, A. Lund, Radiat. Res. 128 (1991) 235–242.
[26] P.O. Samskog, L.D. Kispert, A. Lund, J. Chem. Phys. 77 (1982) 2330–2335.
[27] P.O. Samskog, L.D. Kispert, A. Lund, J. Chem. Phys. 78 (1983) 5790–5794.
[28] G. Vanhaelewyn, B. Jansen, E. Pauwels, E. Sagstuen, M. Waroquier, F. Callens, J. Phys. Chem. A 108 (2004) 3308–3314.
[29] E. Pauwels, V. Van Speybroeck, M. Waroquier, J. Phys. Chem. A 110 (2006) 6504–6513.
[30] C.A. Beevers, T.R.R. McDonald, J.H. Robertson, F. Stern, Acta Crystallogr., Sect. B: Struct. Crystallogr. Cryst. Chem. 5 (1952) 689.
[31] G.M. Brown, H.A. Levy, Science 141 (1963) 921–923.
[32] G.M. Brown, H.A. Levy, Acta Crystallogr., Sect. B: Struct. Crystallogr. Cryst. Chem. 29 (1973) 790–797.
[33] W.H. Nelson, J. Magn. Reson. 38 (1980) 71–78.
[34] A.R. Sørnes, E. Sagstuen, A. Lund, J. Phys. Chem. 99 (1995) 16867–16876.
[35] W. Gordy, Theory and Applications of Electron Spin Resonance, Wiley, New York, 1980.
[36] H.M. McConnell, D.B. Chesnut, J. Chem. Phys. 28 (1958) 107–117.
[37] P.A. Erling, W.H. Nelson, J. Phys. Chem. A 108 (2004) 7591–7595.
[38] W.A. Bernhard, Adv. Radiat. Biol. 9 (1981) 199.
[39] W.A. Bernhard, J. Chem. Phys. 81 (1984) 5928–5935.
[40] R. Declerck, E. Pauwels, V. Van Speybroeck, M. Waroquier, J. Phys. Chem. B, submitted for publication.
[41] CPMD V3.11 Copyright IBM Corp. 1990–2006, Copyright MPI fuer Festkoerperforschung Stuttgart 1997–2001.
[42] J.P. Perdew, Phys. Rev. B 33 (1986) 8822–8824.
[43] A.D. Becke, J. Chem. Phys. 96 (1992) 2155–2160.
[44] D. Vanderbilt, Phys. Rev. B 41 (1990) 7892–7895.
[45] M.J. Frisch, G.W. Trucks, H.B. Schlegel, G.E. Scuseria, M.A. Robb, J.R. Cheesemam, J.J.A. Montgomery, T. Vreven, K.N. Kudin, J.C. Burant, J.M. Millam, S.S. Lyengar, J. Tomasi, V. Barone, B. Mennucci, M. Cossi, G. Scalmani, N. Rega, G.A. Petersson, H. Nakatsuji, M. Hada, M. Ehara, K. Toyota, R. Fukuda, J. Hasegawa, M. Ishida, T. Nakajima, Y. Honda, O. Kitao, H. Nakai, M. Klene, X. Li, J.E. Knox, H.P. Hratchian, J.B. Cross, C. Adamo, J. Jaramillo, R. Gomperts, R.E. Stratmann, O. Yazyev, A.J. Austin, R. Cammi, C. Pomelli, J.W. Ochterski, P.Y. Ayala, K. Morokuma, G.A. Voth, P. Salvador, J.J. Dannenberg, V.G. Zakrzewski, S. Dapprich, A.D. Daniels, M.C. Strain, O. Farkas, D.K. Malick, A.D. Rabuck, K. Raghavachari, J.B. Foresman, J.V. Ortiz, Q. Cui, A.G. Baboul, S. Clifford, J. Cioslowski, B.B. Stefanov, G. Liu, A. Liashenko, P. Piskorz, I. Komaromi, R.L. Martin, D.J. Fox, T. Keith, M.A. Al-Laham, C.Y. Peng, A. Nanayakkara, M. Challacombe, P.M.W. Gill, B. Johnson, W. Chen, M.W. Wong, C. Gonzalez, J.A. Pople, Gaussian 03, Revision B.03, Gaussian, Inc., Pittsburgh, PA, 2003.
[46] A.D. Becke, J. Chem. Phys. 104 (1996) 1040–1046.
[47] R. Krishnan, J.S. Binkley, R. Seeger, J.A. Pople, J. Chem. Phys. 72 (1980) 650–654.
[48] A.D. McLean, G.S. Chandler, J. Chem. Phys. 72 (1980) 5639–5648.
[49] E. Pauwels, V. Van Speybroeck, M. Waroquier, J. Phys. Chem. A 108 (2004) 11321–11332.
[50] E. Pauwels, R. Declerck, V. Van Speybroeck, M. Waroquier, Radiat. Res., accepted for publication.